Supplementary Information for A High-Performance Radiative Cooling Glass Based on Multi-Band Selective Regulation for Synergistic Heat Dissipation and Resistance

Siming Zhao[1], Shuangdui Wu[4], Zhenyu Guo[1], Fan Lan[1], Xueke Wu[1], Ya Huang[1], Ruina Liu[1], Zhuojing Zhao[1], Fei Wang[1], Aike Xi[1], Linan Feng[1], Weiyin Su[1], Kangkang Wang[1], Borong Lin[4], Rufan Zhang[1,2,3,*]

1 Beijing Key Laboratory of Green Chemical Reaction Engineering and Technology, Department of Chemical Engineering, Tsinghua University, Beijing 100084, China.

2 State Key Laboratory of Chemical Engineering and Low-carbon Technology, Department of Chemical Engineering, Tsinghua University, Beijing 100084, China.

3 Ordos Laboratory, Ordos, Inner Mongolia Autonomous Region 010020, China.

4 Key Laboratory of Eco Planning & Green Building, Ministry of Education, Department of Building Science, Tsinghua University, Beijing, 100084, China.

E-mail: zhangrufan@tsinghua.edu.cn

Methods:

Synthesis of the MBSR-RC glass:

Firstly, the PDMS precursor (Sylgard184, Dow Corning) with a curing agent in an appropriate concentration by volume was prepared. The micro-size SiO_2 particles was dispersed in the ethyl acetate via a sonic treatment. Then the PDMS precursor solution and SiO_2-dispersed solution was mixed uniformly. The $CsWO_x$ was sonically dispersed in the ethanol with the concentration of 1 g/1 mL. Then the $CsWO_x$ solution was spray coating on the commercial ITO glass as the substrate. Then, the prepared mixture of PDMS and SiO_2 was blade coated on the substrate with a thickness of 30 μm.

Characterization:

The structure, morphology, and composition characterization of the MBSR-RC glass were obtained by X-ray diffraction (XRD), scanning electron microscopy (SEM), transmission electron microscopy (TEM), Fourier-transform infrared spectroscopy (FTIR) characterizations. XRD patterns were obtained by using Bruker D8 advance diffractometer with Cu-Kα radiation (λ=1.54056Å). SEM images were collected using

JSM 7401F scanning electron microscope (JEOL Ltd., Japan). TEM images were obtained by JEM-2010 transmission electron microscope (JEOL Ltd., Japan). Thermal conductivity was measured by using a thermal constant analyzer (TPS 2500S, Hot Disk) with a 7577 sensor.

Cooling performance test:

Spectral Characterization: The spectral responses of the thermal emitters in the solar spectrum (0.3–2.5 μm) and MIR (2.5–25 μm) wavebands were characterized separately. The former was recorded using an ultraviolet-visible-near-infrared (UV-vis-NIR) spectrophotometer (Cary 7000, Agilent) equipped with an integrating sphere model (Internal DRA-2500, Agilent, barium sulfate as baseline material). During the test, the effect of corresponding substrate was eliminated. The latter was recorded using a Fourier transform infrared spectrometer (FTIR, INVENIO, Bruker) equipped with a gold integrating sphere (A562, Bruker, gold as baseline material) and an attenuated total reflection module (ATR, diamond as baseline material).

Outdoor cooling performance: The cooling performance of different samples was tested by the devices consisting of a sample, K-type thermocouple, and aluminum foil on the insulating foam. The thermocouples were used to record the real-time temperature of samples, which were placed in the center of the box. The real-time environmental conditions were measured and recorded by a weather station, which was located next to the device. The solar irradiation power was measured and recorded by a data-logging solar power meter, which was put near the measured device. And the solar irradiation and ambient temperature are also obtained on the website (https://toolkit.solcast.com.au/). The window-to-wall ratio is about 15%.

Calculation of the optical property

Solar transmission is defined as follows:

$$\overline{T}_{\text{solar}} = \frac{\int_{300\ \text{nm}}^{2500\ \text{nm}} T(\lambda) I_{\text{AM1.5}}(\lambda) \mathrm{d}\lambda}{\int_{300\ \text{nm}}^{2500\ \text{nm}} I_{\text{AM1.5}}(\lambda) \mathrm{d}\lambda}$$

, where $T(\lambda)$ is the transmittance of materials in specific solar regions, $I_{AM1.5}(\lambda)$ is the theoretical solar irradiance intensity.

MIR emissivity in ATW is defined as follows:

$$\bar{\varepsilon}_{\text{ATW}} = \frac{\int_{8\ \mu\text{m}}^{13\ \mu\text{m}} I_{BB}(T,\lambda)\varepsilon(T,\lambda)\mathrm{d}\lambda}{\int_{8\ \mu\text{m}}^{13\ \mu\text{m}} I_{BB}(T,\lambda)\mathrm{d}\lambda}$$

, where $\varepsilon(T, \lambda)$ is the emissivity of materials in specific ATW regions, and $I_{BB}(T, \lambda)$ is the thermal irradiance intensity based on Blackbody radiation law.

MIR emissivity in non-ATW is defined as follows:

$$\bar{\varepsilon}_{\text{non - ATW}} = \frac{\int_{3\ \mu\text{m}}^{8\ \mu\text{m}} I_{BB}(T,\lambda)\varepsilon(T,\lambda)\mathrm{d}\lambda + \int_{13\ \mu\text{m}}^{20\ \mu\text{m}} I_{BB}(T,\lambda)\varepsilon(T,\lambda)\mathrm{d}\lambda}{\int_{3\ \mu\text{m}}^{8\ \mu\text{m}} I_{BB}(T,\lambda)\mathrm{d}\lambda + \int_{13\ \mu\text{m}}^{20\ \mu\text{m}} I_{BB}(T,\lambda)\mathrm{d}\lambda}$$

, where $\varepsilon(T, \lambda)$ is the emissivity of materials in non-ATW, and $I_{BB}(T, \lambda)$ is the thermal irradiance intensity based on Blackbody radiation law.

MIR reflectivity in non-ATW is defined as follows:

$$\bar{R}_{\text{non - ATW}} = 1 - \bar{\varepsilon}_{\text{non - ATW}}$$

The selectivity factor is defined as the ratio of the emissivity in ATW and the emissivity in non-ATW.

The calculation of the thermal calculation:

The temperature inside the buildings in Figure 1 was calculated via the 1D steady heat transfer model, which was depicted in previous literature.[1] This model comprehensively considered the effects of solar irradiance absorption, indoor heat convection, and MIR irradiance heat transfer, which was depicted as equation below.

The indoor temperature would be affected by the irradiance heat transfer and indoor heat convection, including the ambient emissivity (ε_a), stefan-boltzmann constant (σ),

solar transmittance (τ), indoor ambient temperature (T_{air}), solar irradiance absorption of air (α_{air}), solar irradiance power (P_{sun}), the temperature of inner surface (T_{in}), the emissivity of inner surface (ε_{in}), and the indoor convection (h_{in}). The indoor ambient temperature (T_{air}) is defined as follows:

$$\varepsilon_a \sigma T_{air}^4 = \alpha_{air} \tau P_{sun} + \varepsilon_a \varepsilon_{in} \sigma T_{in}^4 + (1-\varepsilon_{in}) \varepsilon_a^2 \sigma T_{air}^4 + h_{in}(T_{in} - T_{air})$$

The temperature of inner surface is calculated as follows, including the thickness (λ), the heat conductivity (k) of the window, and the temperature of the outer surface (T_{out}):

$$\varepsilon_{in} \sigma T_{in}^4 + h_{in}(T_{in} - T_{air}) = \varepsilon_{in} \varepsilon_a \sigma T_{air}^4 + k\frac{T_{out} - T_{in}}{\lambda}$$

The temperature of outer surface is calculated as follows, including heat convection constant (h_{out}), the ambient temperature, and the emissivity of the outer surface (ε):

$$k\frac{T_{out} - T_{in}}{\lambda} + \varepsilon \sigma T_{out}^4 = \varepsilon \varepsilon_a \sigma T_{amb}^4 + h_{out}(T_{amb} - T_{out})$$

Specifically, in summer, the solar irradiance is 1000 $W \cdot m^{-2}$. The ambient temperature is set as 25 °C. The heat convection constant is 10 $W \cdot m^{-2} \cdot K^{-1}$. The heat conductivity is 1 $W \cdot m^{-1} \cdot K^{-1}$, and the thickness of windows is 0.01 m. The solar transmittance, inner emissivity, and outer emissivity of normal glass are 0.9, 0.9, and 0.9, respectively. The solar transmittance, inner emissivity, and outer emissivity of the Low-E glass are 0.5, 0.1, and 0.1, respectively. The solar transmittance, inner emissivity, and outer emissivity of the p-RC glass are 0.5, 0.9, and 0.1, respectively. The solar transmittance, inner emissivity, and outer emissivity of the MBSR-RC glass are 0.5, 0.5, and 0.1, respectively.

And the methods of comsol Multiphysics was also reported in previous literature.[2] The solar absorption of solar heating plate was set as 0.9 to absorb the sunlight and increase the temperature under sunlight. The heating plate was set as a heat with different heating power at night without the sunlight.

The calculation of the scattering cross-section

Lorenz-Mie theory for spheres was utilized to calculate the scattering cross-

section.[3] Wavelength (λ), spherical radius (r), and the complex refractive index (m) of the material need to be used. The ratio of the scattering cross-section to the spherical projection area, i.e. the expression for the scattering coefficient Q_s, is defined as follows:

$$Q_s = \frac{2}{x^2}\sum_{n=0}^{\infty}(2n+1)\left(|a_n|^2 + |b_n|^2\right)$$

, where $x = \frac{2\pi r}{\lambda}$ and a_n and b_n are coefficients defined as follows:

$$a_n = \frac{\psi_n'(mx)\psi_n(x) - m\psi_n(mx)\psi_n'(x)}{\psi_n'(mx)\zeta_n(x) - m\psi_n(mx)\zeta_n'(x)}$$

$$b_n = \frac{m\psi_n'(mx)\psi_n(x) - \psi_n(mx)\psi_n'(x)}{m\psi_n'(mx)\zeta_n(x) - \psi_n(mx)\zeta_n'(x)}$$

The functions $\psi_n(x)$ and $\zeta_n(x)$ are known as Riccati-Bessel functions, which are related to spherical Bessel function $j_n(x)$ and $y_n(x)$as follows:

$$\psi_n(z) = zj_n(z)$$

$$\zeta_n(z) = z\left(j_n(z) - iy_n(z)\right)$$

, where $j_n(x)$ and $y_n(x)$ can be expressed by Bessel function $J_n(x)$ and $Y_n(x)$ as follows:

$$j_n(x) = \sqrt{\frac{\pi}{2x}}J_{n+\frac{1}{2}}(x)$$

$$y_n(x) = \sqrt{\frac{\pi}{2x}}Y_{n+\frac{1}{2}}(x)$$

, where $\psi_n'(x)$ and $\zeta_n'(x)$ can be obtained through recursion as follows:

$$\psi_n'(x) = \psi_{n-1}(x) - \frac{n}{x}\psi_n(x)$$

$$\zeta_n'(x) = \zeta_{n-1}(x) - \frac{n}{x}\zeta_n(x)$$

Usually, we take the first *M* terms for Q_s calculation, where $M = \left\lceil x + 4x^{\frac{1}{3}} + 1 \right\rceil$.

In order to better compare the scattering ability of spheres with different radii for light, the results of each radius obtained from above were divided by the maximum of them so that all the values were enabled to range from 0 to 1.

The theoretical calculation of the PDMS emissivity

The calculation was based on film interference and relevant optical property. Firstly, the PDMS film is considered a system of air/PDMS/air. The response to infrared irradiation is expressed by the complex refractive index, which includes the real part (phase propagation behavior) and imaginary part (absorption behavior) as follows:

$$N(\lambda) = n(\lambda) + ik(\lambda)$$

When the light shed on the interference of air and PDMS or PDMS and air, the transmittance and reflectance can be expressed via Fresnel equation as follows:

$$r_{01} = \frac{N_0 - N_1}{N_0 + N_1}, t_{01} = \frac{2N_0}{N_0 + N_1}$$

$$r_{12} = \frac{N_1 - N_s}{N_1 + N_s}, t_{12} = \frac{2N_1}{N_1 + N_s}$$

Since a thin film has a finite thickness, light accumulates phase as it propagates inside the film. Meanwhile, if the material exhibits optical absorption, this complex phase also contains information on amplitude attenuation and follows the regulation as follows:

$$\delta = \frac{2\pi N_1 d}{\lambda}$$

Light entering the thin film undergoes multiple successive reflections between the front and rear interfaces. Therefore, the total reflection/transmission amplitude does not result from a single reflection/transmission, but from the coherent superposition of all round-trip reflected/transmitted waves, which could be expressed as follows:

$$r = \frac{r_{01} + r_{12}e^{2i\delta}}{1 + r_{01}r_{12}e^{2i\delta}}$$

$$t = \frac{t_{01}t_{12}e^{i\delta}}{1 + r_{01}r_{12}e^{2i\delta}}$$

The energy reflectivity can be derived from the amplitude reflection coefficient,

which represents the fraction of incident energy that is reflected back. Therefore, the reflectivity could be expressed as follows:

$$R = |r|^2$$

The energy transmittance can be obtained from the amplitude transmission coefficient, which refers to the proportion of incident energy that passes through the thin film. The transmissivity could be expressed as follows:

$$T = \frac{Re(N_s)}{Re(N_0)}|t|^2$$

Based on energy conservation law, the absorption the film could be expressed as follows:

$$A(\lambda) = 1 - R(\lambda) - T(\lambda)$$

Finally, attributing to the Kirchhoff's law of thermal radiation, the emissivity of the PDMS film could be obtained as follows:

$$\varepsilon(\lambda) = A(\lambda)$$

The computation of the energy-saving potential

The building energy saving calculation was computed via EnergyPlus, an open-source whole-building energy simulation software. The software takes all loads (equipment, occupants, and lighting) into consideration for occupants' thermal comfort. We used EnergyPlus to calculate the energy consumption of HVAC systems in different China areas by EnergyPlus version 9.4. Different cities were selected to represent the typical climate zones around the world. Here, we used hourly weather data for a typical meteorological year. The apartment model from the previous literature and the US Department of Energy was utilized for simulation. The simulated building was rectangular with 8 stories (length, 25 m; width, 20 m; height, 32 m, windows to wall ratio, 50%). The envelope structure of windows chose the hollow structure of two layers. The heating and cooling loads were calculated all year round. The solar absorption and thermal emissivity of the MBSR-RC glass, normal glass, and low glass was input as measured data, respectively.

The durability measurement the materials:

The UV aging measurement was taken to investigate the degradation of the MBSR-

RC glass under long-time ultraviolet exposure. UV radiation was provided by a UV lamp (LXZ920072) with a power density of ~5 W/m^2, which provided a peak wavelength of ~365 nm.[4] The samples were put under waterdrop impact for 20 hours with a speed of 8 m s^{-1} to test their anti-impact ability in intense rain. And the sample was also immersed totally in the water for 7 days. The optical property of the samples was measured before and after the durability test via the FTIR. The hydrophobicity was obtained via the water contact angle test.

Haze measurement:

Haze is defined as the ratio of the luminous flux of scattered light passing through the sample and deviating from the incident angle by more than 2.5° to the total luminous flux passing through the sample. In this work, haze is obtained through the an ultraviolet-visible-near-infrared (UV-vis-NIR) spectrophotometer (Cary 7000, Agilent) equipped with an integrating sphere model, using the ASTM D-1003-00 method.

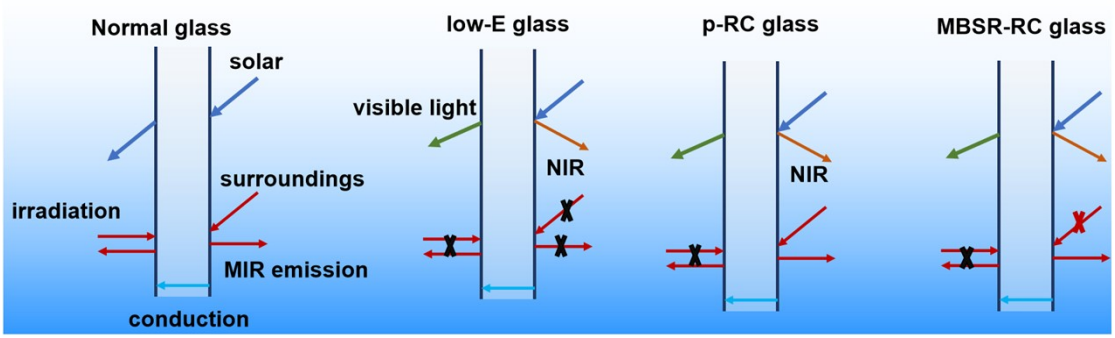

Figure S1. Schematic illustration for heat irradiation transfer of different kinds of glass.

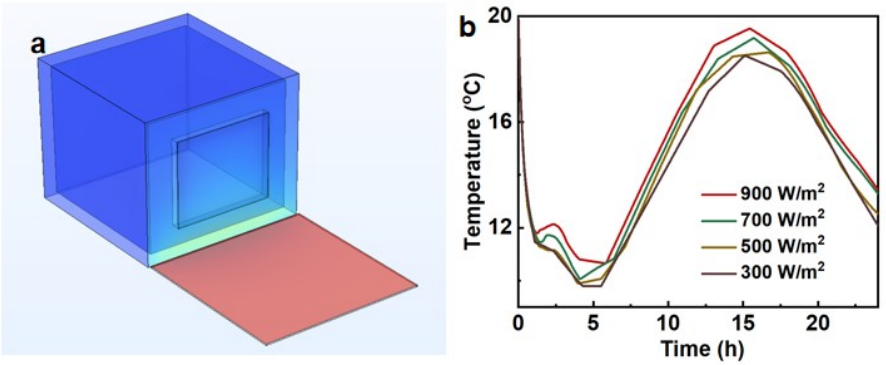

Figure S2. The Comsol Multiphysics® simulation of different glass under sunlight with the solar-absorption plate. (a) The simulation model of a building with glass and heating plate in Comsol Multiphysics. (b) The indoor temperature of a building with Low-E glass near the heating plate in the Comsol simulation.

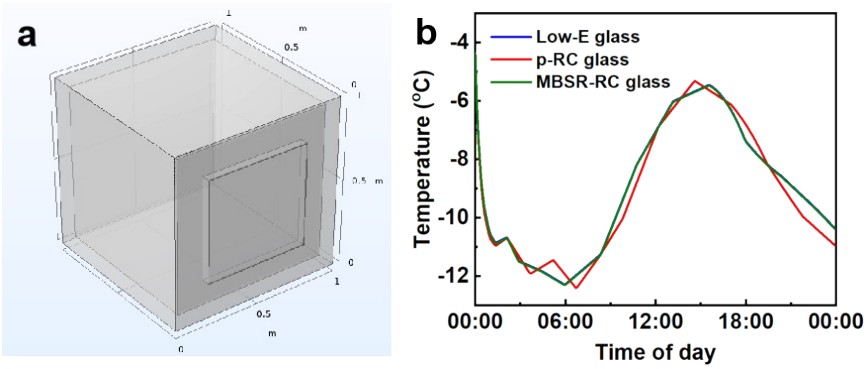

Figure S3. The Comsol Multiphysics® simulation of different glass in winter. (a) The simulation model of a building with glass in Comsol Multiphysics. (b) The indoor temperature of a building in the Comsol simulation.

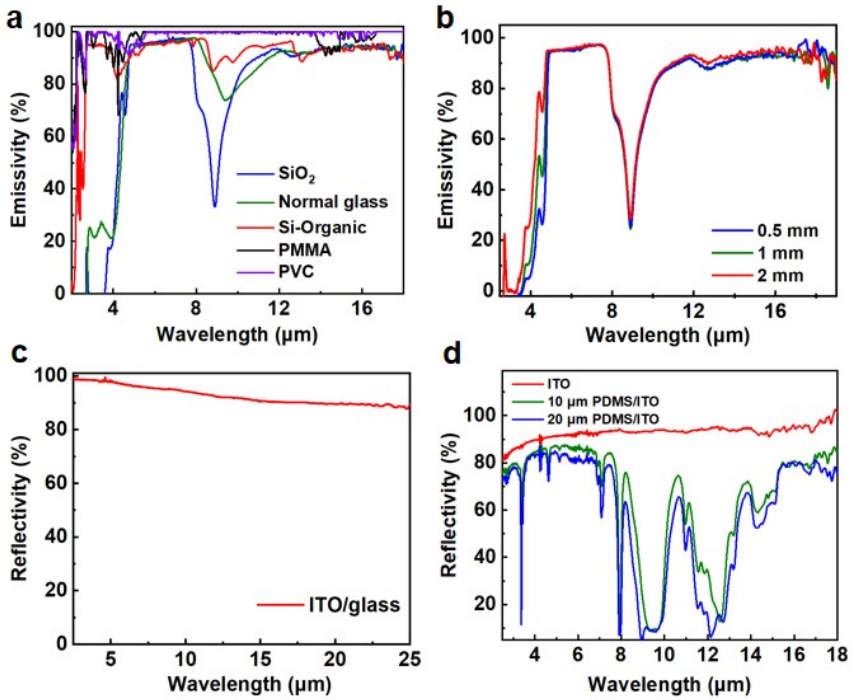

Figure S4. Spectral performance of different substrates. (a) The emissivity of different glass materials in MIR regions. (b) The emissivity of SiO_2 with different thickness in MIR regions. The emissivity of PDMS with different thickness in MIR regions. The reflectivity in MIR regions of (c) ITO glass, and (d) PDMS on ITO glass.

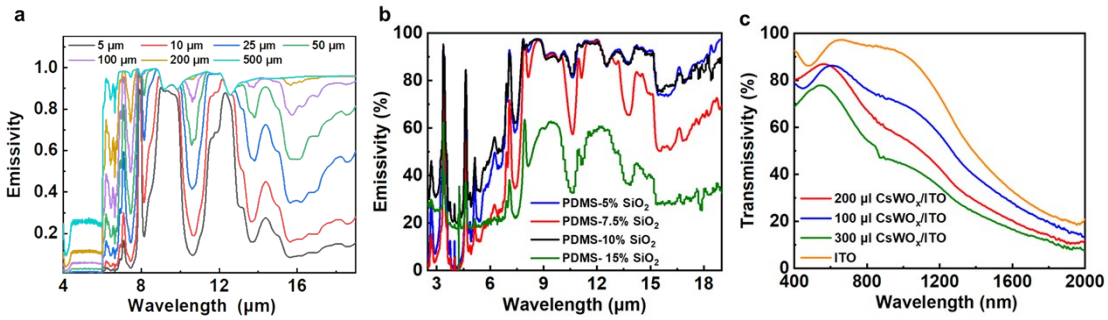

Figure S5. The spectral performance of the additives. (a) Simulated MIR emissivity of PDMS with different thickness. (b) MIR emissivity of the PDMS with different concentration of SiO_2 micro-particles. (c) The solar transmissivity of ITO glass with different contents of $CsWO_x$.

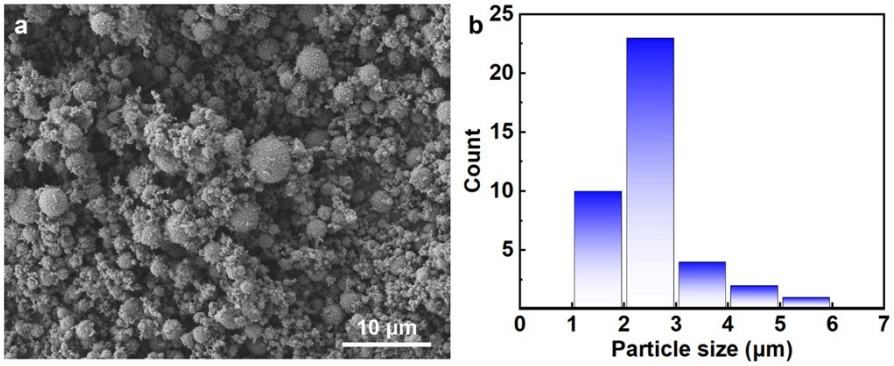

Figure S6. The morphology of SiO_2 micro-particles. (a) SEM image. (b) Particle size distribution.

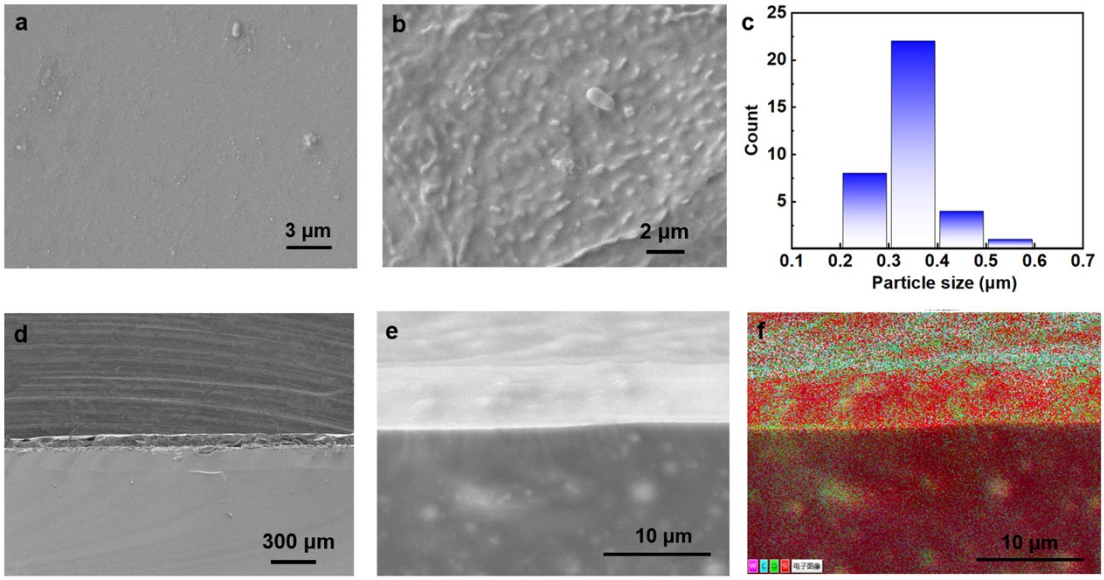

Figure S7. Morphology and structure characterization of the MBSR-RC glass. SEM images of (a, b) MBSR-RC glass surface. (c) Appearance particle size distribution of figure S7b SEM images of (d, e) the cross section and (f) corresponding EDS Mapping of the MBSR-RC glass.

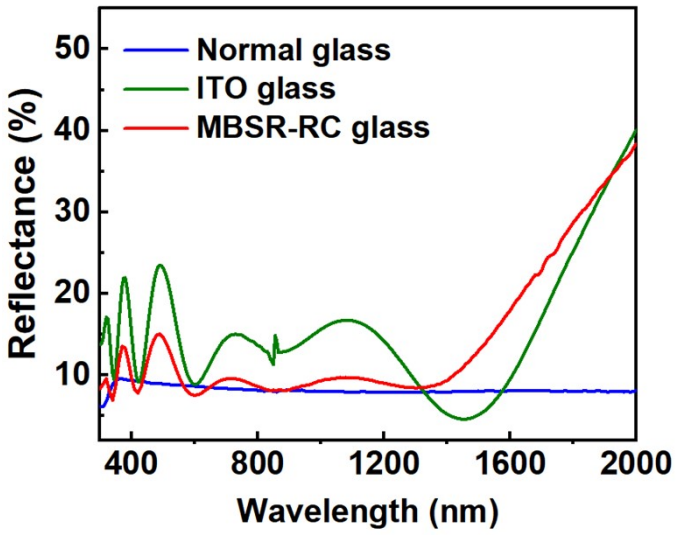

Figure S8. Solar reflectance of normal glass, Low-E glass, and MBSR-RC glass.

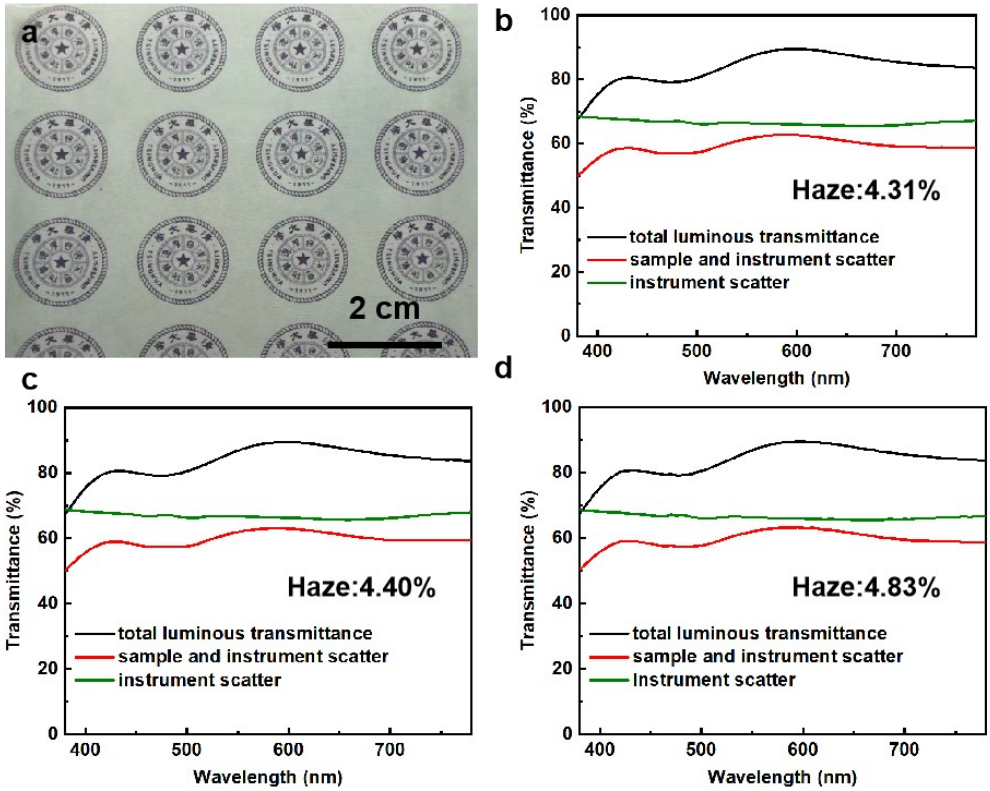

Figure S9. (a) Digital photo of MBSR-RC glass. (b-d) Haze measurement of the MBSR-RC glass.

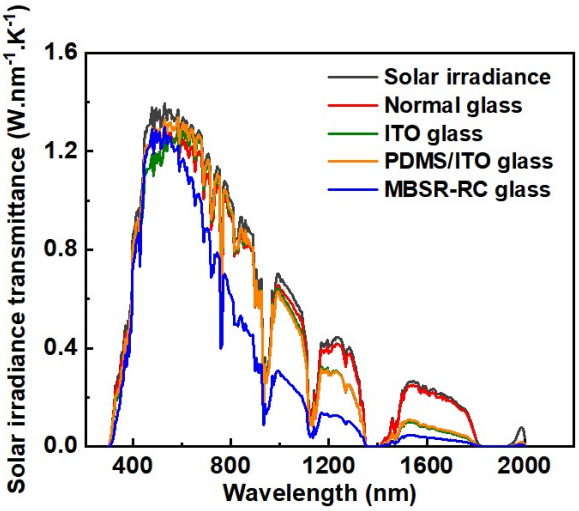

Figure S10. Solar irradiance transmittance of different glass.

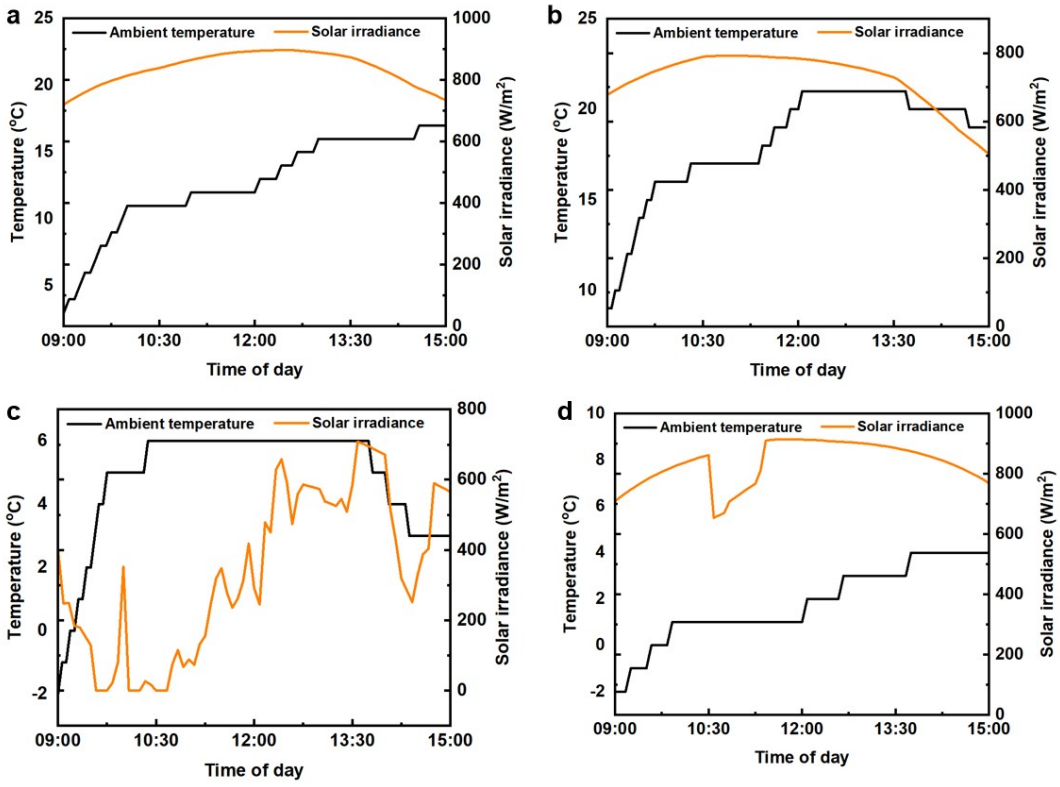

Figure S11. Solar irradiance and ambient temperature of (a) Figure 3b, (b) Figure 3c, (c) Figure 3e, and (d) Figure 3f.

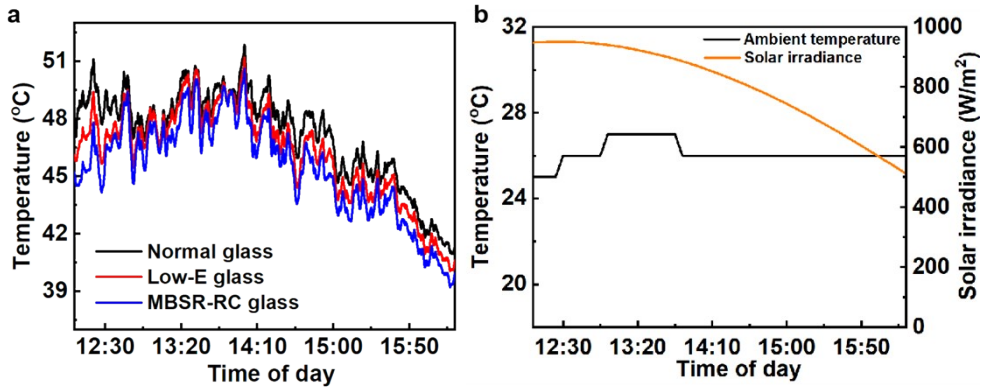

Figure S12. (a) Temperature measurements of the thermal equipment with different glass types positioned vertically relative to the ground. (b) Its solar irradiance and ambient temperature.

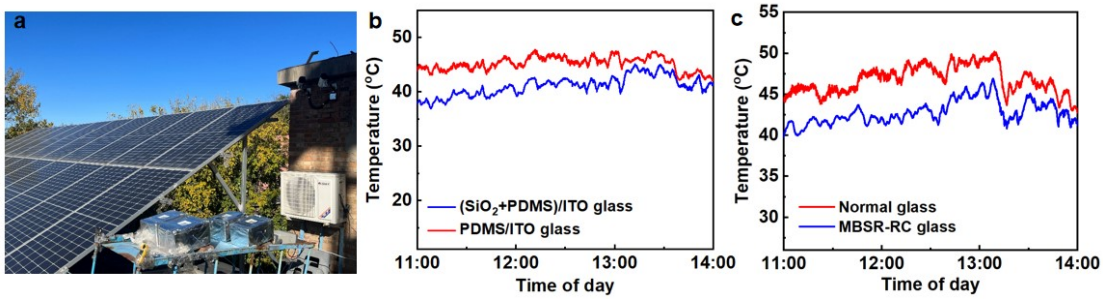

Figure S13. The temperature measurement of the different. (a) Digital photos of the thermal measurement equipment. The internal temperature of the equipment with (b, c) PDMS/ITO glass, (PDMS+SiO_2)/ITO glass, normal glass, and MBSR-RC glass.

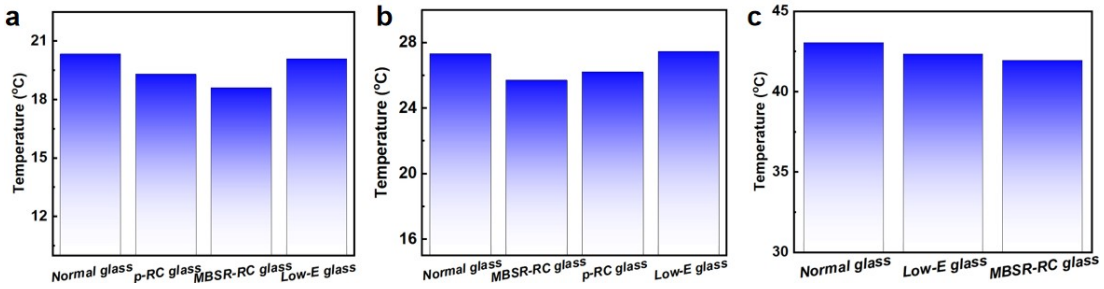

Figure S14. Average temperature of different outdoor experiments in (a) Figure 3b (b) Figure 3c, (c) Figure S11(a).

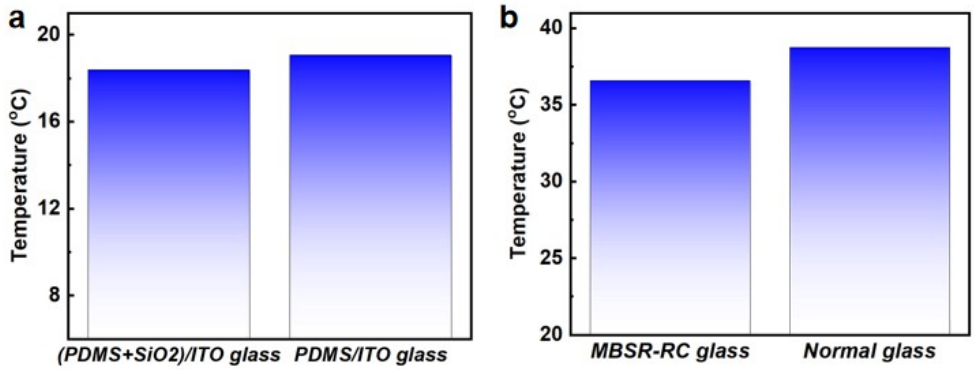

Figure S15. Average temperature of different outdoor experiments in (a) Figure S12b (b) Figure S12c.

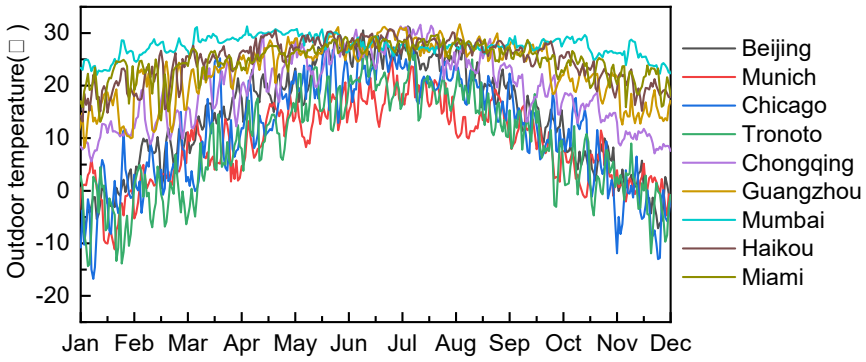

Figure S16. The environmental conditions of different cities in the EnergyPlus Calculation.

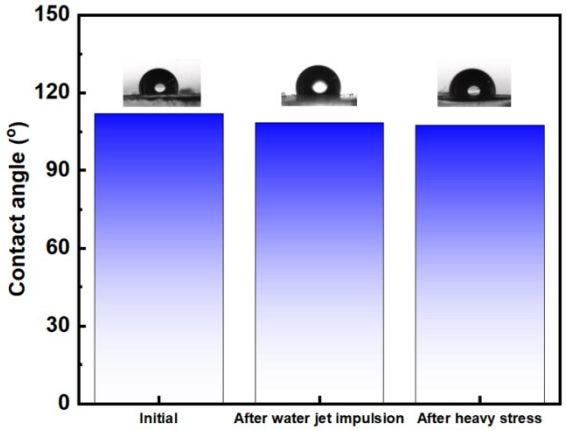

Figure S17. The contact angle of the MBSR-RC glass before and after the water jet impulsion and heavy stress, respectively.

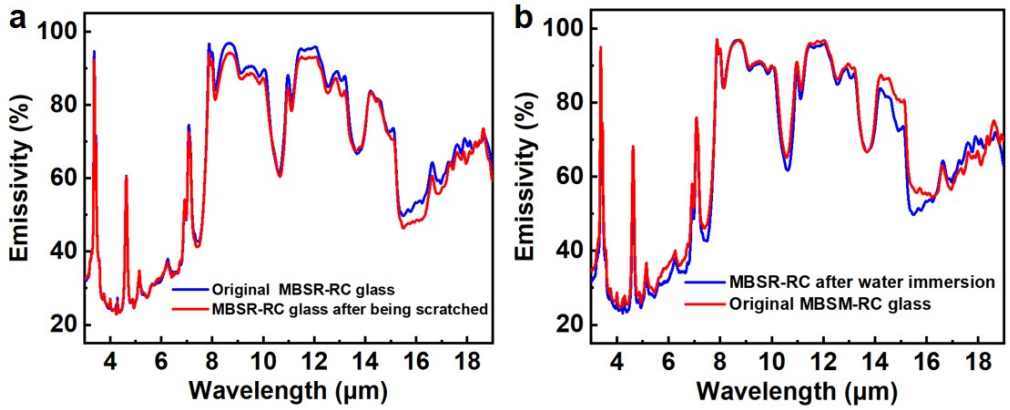

Figure S18. The stability test of the MBSR-RC glass. (a) The emissivity of the MBSR-RC glass before and after being scratched. (b) The emissivity of the MBSR-RC glass before and after the water immersion.

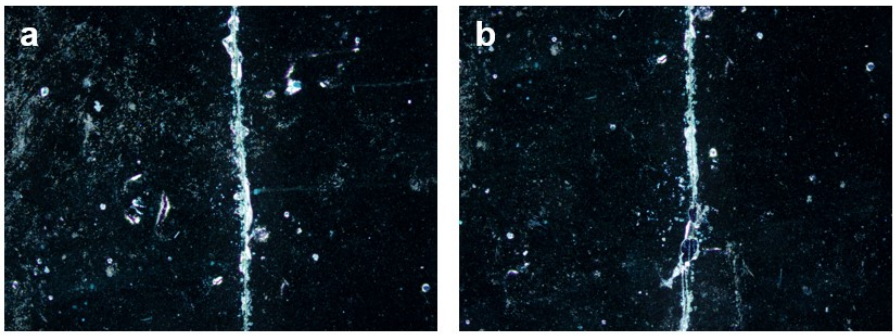

Figure S19 The optical image of the MBSR-RC glass (a) before and (b) after the tape pulling.

Table S1. Comparison between the MBSR-RC glass and other samples in the reported literature.

Materials	Method	Transmissivity in VIS	Transmissivity in NIR	Emissivity in MIR regions	Selective or not	Selective factor	Reference
FEP/ITO/Ag/ITO	Sputtering	65.20%	47.4%(reflectivity)	97.50%	Broad	1.3	[5]
W-VO_2@SiO_2/glass	Spray coatings	43.10%	\	94%	Broad(adaptive)	1.1	[6]
T-RC	Sputtering	68.92%	20.85%	90%	Broad	1.25	[7]
Si_3N_4/ITO glass	Sputtering	76%	20%	25%	Angle-dependent	/	[8]
PDMS/TiO_2/Ag/TiO_2	Sputtering	70%	20%	90%	Broad	1.2	[9]
PDLC/PET	Spray coatings	30%	50%	80%	Broad	1.1	[10]
PDMS/Ag/SiO_2/TiO_2	Sputtering	65.40%	14.20%	85.80%	Broad	/	[11]
Tin oxide in CA	Sputtering	80%	60%	/	Broad	1.4	[12]
Glass/TiO_2/Ag/TiO_2	beam evaporation	80%	15%	90%	Broad	1.1	[13]
CWA/PVA/ITO glass	Scrap coating	56.80%	5.40%	91%	Broad	\	[14]
AgNWs/CA	Spray coatings	40%	30%	95%	Broad	1.0	[15]
(PDMS+SiO_2)/$CsWO_x$/ITO	**Scrap coating**	**85%**	**28%**	**87%**	**Selective**	**1.58**	**This work**

Table S2. The EnergyPlus calculation settings.

parameter	setting
Envelope	The heat transfer coefficient of the external wall and roof is 0.45W/(m^2·K)
Indoor load	occupancy density: 10 m^2 /person lighting power density: 9 W/ m^2 equipment power density: 15 W/ m^2
Working schedule	8:00 to 18:00 form Monday to Friday
Design parameter	The heating and air conditioning temperatures in the room were set to 20°C and 24°C
Lighting control	Linear/off strategy, target illuminance at 300lx
Equipment for HVAC	Heat pumps are used for heating and cooling, both with COP

(coefficient of performance) 2.5

Table S3. The energy consumption of buildings with different types of windows in Beijing.

Type	**Cooling consumption/(kWh/m^2)**	**Heating consumption/(h/m^2)**
MBSR-RC windows	36.9	21.7
Normal windows	37.5	26.9
Low-E windows	39.6	22.2

Table S4. The energy consumption of buildings with different types of windows in hot cities.

City	Type	Energy consumption/(kWh/m^2)
Beijing	MBSR-RC windows	60.3
	Low-E windows	61.8
Chongqing	MBSR-RC windows	47.5
	Low-E windows	50.5
Munich	MBSR-RC windows	49.3
	Low-E windows	57.2
Chicago	MBSR-RC windows	62.4
	Low-E windows	70.4
Guangzhou	MBSR-RC windows	67.5
	Low-E windows	70.12
Toronto	MBSR-RC windows	62.0
	Low-E windows	71.5

Reference:

(1) Huang, Y.; Wu, S.; Zhao, S.; Guo, Z.; Zhao, Z.; Wu, X.; Wang, B.; Wang, F.; Xi, A.; Lan, F.; et al. A novel liquid flow electrochromic smart window for all-year-round dynamic photothermal regulation. *Energy Environ. Sci.* **2025**, *18* (4), 1824-1834.

(2) Xu, J.; Wu, X.; Li, Y.; Zhao, S.; Lan, F.; Xi, A.; Huang, Y.; Ding, Y.; Zhang, R.

High-Performance Radiative Cooling Sunscreen. *Nano Letters* **2024**, *24* (47), 15178-15185.

(3) Hergert, W.; Wriedt, T. The Mie theory: basics and applications. 2012.

(4) Zhao, X.; Li, T.; Xie, H.; Liu, H.; Wang, L.; Qu, Y.; Li, S. C.; Liu, S.; Brozena, A. H.; Yu, Z.; et al. A solution-processed radiative cooling glass. *Science* **2023**, *382* (6671), 684-691.

(5) Jung, Y.; Kim, J.-S.; Bang, J.; Choi, S. H.; Kwon, K.; Lee, M. J.; Oh, I.-K.; Song, J.; Lee, J.; Ko, S. H. Energy-saving window for versatile multimode of radiative cooling, energy harvesting, and defrosting functionalities. *Nano Energy* **2024**, *129*, 110004.

(6) Wang, Z.; Liang, J.; Lei, D.; Jiang, C.; Yang, Z.; Yang, G.; Zhang, D.; Zhang, L.; Zhang, C.; Bai, Y. Temperature-adaptive smart windows with passive transmittance and radiative cooling regulation. *Appl. Energy* **2024**, *369*, 123619.

(7) Zou, H.; Wang, C.; Yu, J.; Huang, D.; Yang, R.; Wang, R. Eliminating greenhouse heat stress with transparent radiative cooling film. *Cell Rep. Phys. Sci.* **2023**, *4* (8), 101539.

(8) Bae, M.; Kim, D. H.; Kim, S.-K.; Song, Y. M. Transparent energy-saving windows based on broadband directional thermal emission. *Nanophotonics* **2024**, *13* (5), 749-761.

(9) Li, Y.; Chen, X.; Yu, L.; Pang, D.; Yan, H.; Chen, M. Janus Interface Engineering Boosting Visibly Transparent Radiative Cooling for Energy Saving. *ACS Appl. Mater. Interfaces* **2023**, *15* (3), 4122-4131.

(10) Ma, C.; Zhang, Z.; Yang, Y.; Wang, P.; Yu, M.; Gao, Y.; Wang, Q.; Xiao, J.; Zou, C.; Yang, H. A Smart Window with Passive Radiative Cooling and Switchable Near-Infrared Light Transmittance via Molecular Engineering. *ACS Appl. Mater. Interfaces* **2024**, *16* (19), 25343-25352.

(11) Nan, H.; Xiong, P.; Zhong, G.-J.; Li, Y.; Li, R.; Niu, J.-H.; Lei, J.; Li, Z.-M. Ag/SiO2 and Ag/TiO2 Nanoscale-Thick Layers as Hyperbolic Metamaterials for Transparent Radiative Cooling Glass Design. *ACS Appl. Nano Mater.* **2024**, *7* (14), 17111-17119.

(12) Park, S.; Pal, S. K.; Otoufat, T.; Kim, G. Radiative-Cooling Composites with Enhanced Infrared Emissivity by Structural Infrared Scattering through Indium Tin Oxide Nanoparticles in a Polymer Matrix. *ACS Appl. Mater. Interfaces* **2023**, *15* (12), 16026-16033.

(13) Lee, G.; Kang, H.; Yun, J.; Chae, D.; Jeong, M.; Jeong, M.; Lee, D.; Kim, M.; Lee, H.; Rho, J. Integrated triboelectric nanogenerator and radiative cooler for all-weather transparent glass surfaces. *Nat. Commun.* **2024**, *15* (1), 6537.

(14) Hu, L.; Wang, C.; Zhu, H.; Zhou, Y.; Li, H.; Liu, L.; Ma, L. Adaptive Thermal Management Radiative Cooling Smart Window with Perfect Near-Infrared Shielding. *Small* **2024**, *20* (30), 2306823.

(15) Zhou, C.; Julianri, I.; Wang, S.; Chan, S. H.; Li, M.; Long, Y. Transparent Bamboo with High Radiative Cooling Targeting Energy Savings. *ACS Materials Letters* **2021**, *3* (6), 883-888.